The Astrophysical Journal, 661:236–249, 2007 May 20
© 2007. The American Astronomical Society. All rights reserved. Printed in U.S.A.

H.E.S.S. OBSERVATIONS OF THE SUPERNOVA REMNANT RX J0852.0−4622: SHELL-TYPE MORPHOLOGY AND SPECTRUM OF A WIDELY EXTENDED VERY HIGH ENERGY GAMMA-RAY SOURCE

F. Aharonian,[1] A. G. Akhperjanian,[2] A. R. Bazer-Bachi,[3] M. Beilicke,[4] W. Benbow,[1] D. Berge,[1,5]
K. Bernlöhr,[1,6] C. Boisson,[7] O. Bolz,[1] V. Borrel,[3] I. Braun,[1] A. M. Brown,[8] R. Bühler,[1] I. Büsching,[9]
S. Carrigan,[1] P. M. Chadwick,[8] L.-M. Chounet,[10] G. Coignet,[11] R. Cornils,[4] L. Costamante,[1,12]
B. Degrange,[10] H. J. Dickinson,[8] A. Djannati-Ataï,[13] L. O'C. Drury,[14] G. Dubus,[10] K. Egberts,[1]
D. Emmanoulopoulos,[15] P. Espigat,[13] F. Feinstein,[16] E. Ferrero,[15] A. Fiasson,[16] M. D. Filipovic,[17,18]
G. Fontaine,[10] Y. Fukui,[19] Seb. Funk,[6] S. Funk,[1] M. Füßling,[6] Y. A. Gallant,[16] B. Giebels,[10]
J. F. Glicenstein,[20] P. Goret,[20] C. Hadjichristidis,[8] D. Hauser,[1] M. Hauser,[15] G. Heinzelmann,[4] G. Henri,[21]
G. Hermann,[1] J. A. Hinton,[1,15] J. S. Hiraga,[22] A. Hoffmann,[23] W. Hofmann,[1] M. Holleran,[9] S. Hoppe,[1]
D. Horns,[23] Y. Ishisaki,[24] A. Jacholkowska,[16] O. C. de Jager,[9] E. Kendziorra,[23] M. Kerschhaggl,[6]
B. Khélifi,[1,10] Nu. Komin,[16] A. Konopelko,[6,25] K. Kosack,[1] G. Lamanna,[11] I. J. Latham,[8] R. Le Gallou,[8]
A. Lemière,[13] M. Lemoine-Goumard,[10,26] T. Lohse,[6] J. M. Martin,[7] O. Martineau-Huynh,[27] A. Marcowith,[3]
C. Masterson,[1,12] G. Maurin,[13] T. J. L. McComb,[8] E. Moulin,[16] Y. Moriguchi,[1,19] M. de Naurois,[27]
D. Nedbal,[28] S. J. Nolan,[8] A. Noutsos,[8] K. J. Orford,[8] J. L. Osborne,[8] M. Ouchrif,[12,27] M. Panter,[1]
G. Pelletier,[21] S. Pita,[13] G. Pühlhofer,[15] M. Punch,[13] S. Ranchon,[11] B. C. Raubenheimer,[9] M. Raue,[4]
S. M. Rayner,[8] A. Reimer,[29] J. Ripken,[4] L. Rob,[28] L. Rolland,[20] S. Rosier-Lees,[11] G. Rowell,[1] V. Sahakian,[2]
A. Santangelo,[23] L. Saugé,[21] S. Schlenker,[6] R. Schlickeiser,[29] R. Schröder,[29] U. Schwanke,[6,26]
S. Schwarzburg,[23] S. Schwemmer,[15] A. Shalchi,[29] H. Sol,[7] D. Spangler,[8] F. Spanier,[29] R. Steenkamp,[30]
C. Stegmann,[31] G. Superina,[10] P. H. Tam,[15] J.-P. Tavernet,[27] R. Terrier,[13] M. Tluczykont,[10,12]
C. van Eldik,[1] G. Vasileiadis,[16] C. Venter,[9] J. P. Vialle,[11] P. Vincent,[27]
H. J. Völk,[1] S. J. Wagner,[15] and M. Ward[8]

Received 2006 September 6; accepted 2006 December 15

ABSTRACT

The shell-type supernova remnant RX J0852.0−4622 was observed with the High Energy Stereoscopic System (H.E.S.S.) of atmospheric Cerenkov telescopes between 2004 December and 2005 May for a total observation time of 33 hr, above an average gamma-ray energy threshold of 250 GeV. The angular resolution of ~0.06° (for events triggering three or four telescopes) and the large field of view of H.E.S.S. (5° diameter) are well adapted to studying the morphology of the object in very high energy gamma rays, which exhibits a remarkably thin shell very similar to the features observed in the radio range and in X-rays. The spectral analysis of the source from 300 GeV to 20 TeV is also presented. Finally, the possible origins of the very high energy gamma-ray emission (inverse Compton scattering by electrons or the decay of neutral pions produced by proton interactions) are discussed, on the basis of morphological and spectral features obtained at different wavelengths.

Subject headings: gamma rays: observations — ISM: individual (G266.2−1.2, RX J0852.0−4622, Vela Junior) — supernova remnants

Online material: color figures

---

[1] Max-Planck-Institut für Kernphysik, Heidelberg, Germany.

[2] Yerevan Physics Institute, Yerevan, Armenia.

[3] Centre d'Etude Spatiale des Rayonnements, CNRS/UPS, Toulouse, France.

[4] Universität Hamburg, Institut für Experimentalphysik, Hamburg, Germany.

[5] Now at CERN, Geneva, Switzerland.

[6] Institut für Physik, Humboldt-Universität zu Berlin, Germany.

[7] LUTH, UMR 8102 du CNRS, Observatoire de Paris, Section de Meudon, France.

[8] University of Durham, Department of Physics, Durham DH1 3LE, UK.

[9] Unit for Space Physics, North-West University, Potchefstroom, South Africa.

[10] Laboratoire Leprince-Ringuet, IN2P3/CNRS, Ecole Polytechnique, Palaiseau, France.

[11] Laboratoire d'Annecy-le-Vieux de Physique des Particules, IN2P3/CNRS, 110 F-74941 Annecy-le-Vieux Cedex, France.

[12] European Associated Laboratory for Gamma-Ray Astronomy, jointly supported by CNRS and MPG.

[13] APC, Paris Cedex 05, France 7164 (CNRS, Observatoire de Paris).

[14] Dublin Institute for Advanced Studies, Dublin, Ireland.

[15] Landessternwarte, Königstuhl, Heidelberg, Germany.

[16] Laboratoire de Physique Théorique et Astroparticules, IN2P3/CNRS, Université Montpellier II, France.

[17] University of Western Sidney, Penrith South DC, NSW 1797, Australia.

[18] Australia Telescope National Facility, CSIRO, Epping, NSW 1710, Australia.

[19] Department of Astrophysics, Nagoya University, Chikusa-ku, Nagoya 464-8602, Japan.

[20] DAPNIA/DSM/CEA, CE Saclay, Gif-sur-Yvette, France.

[21] Laboratoire d'Astrophysique de Grenoble, INSU/CNRS, Université Joseph Fourier, France.

[22] RIKEN (The Institute of Physical and Chemical Research) 2-1, Hirosawa, Wako, Saitama 351-0198, Japan.

[23] Institut für Astronomie und Astrophysik, Universität Tübingen, Sand 1, D 72076 Tübingen, Germany.

[24] Department of Physics, Tokyo Metropolitan University, Minami-Osawa, Hachioji, Tokyo 192-0397, Japan.

[25] Now at Purdue University, Department of Physics, West Lafayette, IN 47907-2036.

[26] Correspondence and requests for material should be sent to lemoine@poly.in2p3.fr and schwanke@physik.hu-berlin.de.

[27] Laboratoire de Physique Nucléaire et de Hautes Energies, Universités Paris VI et Paris VII, France.

[28] Institute of Particle and Nuclear Physics, Charles University, Prague, Czech Republic.

[29] Institut für Theoretische Physik, Lehrstuhl IV, Ruhr-Universität Bochum, Germany.

[30] University of Namibia, Windhoek, Namibia.

[31] Universität Erlangen-Nürnberg, Physikalisches Institut, D 91058 Erlangen, Germany.

1. INTRODUCTION

Shell-type supernova remnants (SNRs) have long been considered as prime candidates for accelerating cosmic rays up to at least 100 TeV, but until recently, this statement was only supported by indirect evidence, namely nonthermal X-ray emission interpreted as synchrotron radiation from very high energy (VHE) electrons in a few objects (Koyama et al. 1995, 1997). A more direct proof is provided by the emission of high-energy gamma rays produced either by inverse Compton (IC) scattering of high-energy electrons on ambient photons or by nuclear interactions of high-energy protons or ions in the interstellar medium and subsequent π^0 meson decays. However, in the 100 MeV–30 GeV energy range, the Energetic Gamma-Ray Experiment Telescope (EGRET) on board the *Compton Gamma Ray Observatory* could not provide an unambiguous detection of a shell-type SNR, due to its poor angular resolution and to the difficulty of separating signals of extended objects from the diffuse Galactic gamma-ray background. In the very high energy range (>200 GeV) on the other hand, the situation is more favorable (Drury et al. 1994): recent imaging atmospheric Cerenkov telescopes have achieved angular resolutions of the order of a few arcminutes and the diffuse background is expected to decrease more rapidly with energy than the gamma-ray signal. The first confirmed gamma-ray signal from a shell-type SNR was that of RX J1713.7−3946 detected by the CANGAROO I and CANGAROO II experiments (Muraishi et al. 2000; Enomoto et al. 2002), as well as by the H.E.S.S. Collaboration (Aharonian et al. 2004c). The latter experiment provided the first detailed morphological and spectral study of this source (Aharonian et al. 2006). A second shell-type SNR, RX J0852.0−4622 (also named G266.2−1.2), was recently detected by Cerenkov telescopes: the announcement of a signal from the northwestern part by the CANGAROO collaboration (Katagiri et al. 2005) was shortly followed by the publication of a complete gamma-ray map of this object by the H.E.S.S. collaboration (Aharonian et al. 2005b), making it the largest extended source (2° angular diameter) ever resolved by a Cerenkov telescope. This previous H.E.S.S. result was obtained from a short observation campaign (3.2 hr) in 2004. In this article, we present the results of much longer observations of this source in 2005 (~20 hr) with the full H.E.S.S. array.

RX J0852.0−4622 is located in the southeastern corner of the Vela SNR and its study in X-rays as well as in radio is complicated by the superposition of the highly structured emission of the Vela remnant. Its discovery in the *ROSAT* All Sky Survey (Aschenbach 1998) relied on the restriction to energies greater than 1.3 keV where the signal stands out above the soft thermal emission from the Vela SNR. In X-rays, RX J0852.0−4622 appears as a roughly circular disk with a diameter of 2° with a brightening toward the northwestern, western, and southeastern rims.

Since its discovery, its distance and age have been a matter of controversy. Low values of these quantities have been inferred from the detection by COMPTEL (Iyudin et al. 1998) of the 1.157 MeV gamma-ray line of ^{44}Ca due to the decay chain $^{44}\mathrm{Ti} \rightarrow {}^{44}\mathrm{Sc} \rightarrow {}^{44}\mathrm{Ca}$ characterized by the ^{44}Ti lifetime, whose average value, based on measurements by independent groups, is 86.6 ± 1.4 yr (Hashimoto et al. 2001). On the basis of the ^{44}Ti yield and of the X-ray diameter, an age of ~680 yr and a distance of ~200 pc, thus close to that of the Vela remnant, was proposed (Aschenbach et al. 1999). It should be noted that this result was obtained by adopting a mean expansion velocity of 5000 km s^{-1} based on the assumption of a purely thermal X-ray spectrum. However, further observations of the brightest parts of the shell by *ASCA* (Tsunemi et al. 2000; Slane et al. 2001), *XMM-Newton* (Iyudin et al. 2005), and *Chandra* (Bamba et al. 2005a) demonstrated the nonthermal nature of the X-ray emission. In this framework, different models interpreting the X-ray spectrum yield absorbing column densities for RX J0852.0−4622 that are significantly larger than that of the Vela SNR. Moreover, the significance level of the ^{44}Ti yield was later questioned in a reanalysis of COMPTEL data (Schönfelder et al. 2000). The Sc-K emission at about 4 keV expected from the ^{44}Ti yield is also controversial: evidence for this line was first claimed from *ASCA* SIS0 data (Tsunemi et al. 2000), but not confirmed by SIS1 data, from which only an upper limit could be deduced (Slane et al. 2001), whereas a detection at the 4 σ level was obtained from *XMM-Newton* data (Iyudin et al. 2005). The doubt on the detection of the ^{44}Ca and ^{44}Sc lines thus affects the interpretation of RX J0852.0−4622 as a young and nearby SNR.

In contrast, on the basis of the absorbing column density deduced from the X-ray spectrum, Slane et al. (2001) argue in favor of a distance much larger than 200 pc, with the restriction that the remnant be in front of the Vela Molecular Ridge. Otherwise, this concentration of giant molecular clouds, revealed by CO data and located at a distance of ~1–2 kpc, should produce significant absorption in X-rays in the eastern rim of RX J0852.0−4622 at a level which is not observed. New estimates of the age and distance of this source were recently proposed by Bamba et al. (2005a) on the basis of the observation of very thin hard X-ray filaments in the northwestern edge with the high angular resolution of the *Chandra* satellite. Using an empirical relation (Bamba et al. 2005b) between the filament width on the downstream side of the shock w_d, the roll-off frequency ν_{roll} of the synchrotron spectrum, and the SNR age, the authors derive an age in the range of 420–1400 yr and a distance of 0.26–0.50 kpc.

The possible presence of a compact remnant of the supernova explosion at the center of RX J0852.0−4622, first suggested from *ROSAT* observations (Aschenbach 1998), was confirmed by *BeppoSAX* (Mereghetti 2001) and *Chandra* (Pavlov et al. 2001; Kargaltsev et al. 2002); if this object is interpreted as a neutron star, as proposed by Chen & Gehrels (1999), RX J0852.0−4622 would be the remnant of a core-collapse supernova. The absorbing column density obtained from the spectrum of this central object is also significantly higher (Kargaltsev et al. 2002) than those measured for the Vela remnant, supporting larger distances as suggested by Slane et al. (2001). However, Reynoso et al. (2006) recently interpreted the radio counterpart of the central object as due to a planetary nebula; therefore, RX J0852.0−4622 may also be the result of a thermonuclear explosion.

To summarize, there remains a large uncertainty on the distance of RX J0852.0−4622; this object could be as close as the Vela SNR (~290 pc) and possibly in interaction with Vela, or as far as the Vela Molecular Ridge (~1 kpc). Even the nature of the explosion of the progenitor remains unclear. In addition, the superposition of the Vela SNR and RX J0852.0−4622 makes the interpretation of radio and X-ray data difficult. On the other hand, due to its very weak radio emission (Combi et al. 1999; Duncan & Green 2000) and to the nonthermal nature of its X-ray spectrum, RX J0852.0−4622 shows remarkable similarities with RX J1713−3946, also detected in the very high energy range.

This article is organized as follows. In § 2, the main characteristics of the H.E.S.S. telescope array are reviewed and the RX J0852.0−4622 data set is described. Section 3 is devoted to the analysis method (gamma-ray selection, angular resolution, and spectral resolution). Results on the gamma-ray morphology of the source are given in § 4, whereas § 5 is concerned with the spectral analysis. Section 6 reviews and summarizes observations relevant to the multiwavelength study of this object, in particular from the X-ray and radio bands. Section 7 attempts to derive some general constraints on the energetics and emission mechanisms in this source; §§ 8 and 9 then discuss the electronic and hadronic scenarios, respectively, and finally in § 10 we draw some general conclusions.

2. H.E.S.S. OBSERVATIONS

H.E.S.S. is an array of four 13 m diameter imaging Cerenkov telescopes located in the Khomas Highlands in Namibia, 1800 m above sea level (Hinton 2004). Each telescope has a tessellated mirror with an area of 107 m^2 (Bernlöhr et al. 2003) and is equipped with a camera comprising 960 photomultipliers (Vincent et al. 2003), covering a field of view of 5° diameter. During the observations, an array level hardware trigger requires each shower to be observed by at least two telescopes within a coincidence window of 60 ns (Funk et al. 2004). Due to the efficient rejection of hadronic showers provided by stereoscopy, the complete system (operational since 2003 December) can detect point sources at flux levels of about 1% of the Crab Nebula flux near zenith with a significance of 5 σ in 25 hr of observation. This high sensitivity, the angular resolution of a few arcminutes, and the large field of view make H.E.S.S. ideally suited for the study of the gamma-ray morphology of extended sources.

The region of the SNR RX J0852.0−4622 was observed with the complete H.E.S.S. array between 2004 December and 2005 May for a total observation time of 33 hr of ON-source runs. The data were recorded in runs of typical 28 minute duration in the so-called "wobble mode," where the source is offset from the center of the field of view. The offset angles both in right ascension and declination (±0.7°, ±1.1°, and ±1.56°) were chosen in order to provide a full coverage of this widely extended SNR. In order to reduce systematic effects due to varying observational conditions, quality selection criteria were applied on a run-by-run basis resulting in a total of 20 hr of high-quality data at zenith angles between 20° and 50° (with an average of 30°). The energy threshold of the system increases with the zenith angle: for the observations presented here, the average threshold was around 250 GeV.

3. ANALYSIS TECHNIQUE

The data were calibrated as described in detail in Aharonian et al. (2004a). In a first stage, a standard image cleaning was applied to shower images to remove the contamination due to the night sky background. Several independent analysis methods are used within the H.E.S.S. Collaboration (de Naurois et al. 2005) to cross-check all results. The results presented in this paper were obtained using a 3D modeling of the light-emitting region of an electromagnetic air shower, a method referred to as "the 3D model analysis" (Lemoine-Goumard et al. 2005). All results were verified and confirmed using the standard H.E.S.S. analysis described in detail in Aharonian et al. (2005a). We briefly recall the main characteristics of these methods:

1. The standard stereoscopic analysis is based on the Hillas parameters of shower images (Aharonian et al. 2005a). The incident direction and the shower impact on the ground are reconstructed from the image axes, whereas parameters directly related to the widths and lengths of the images (mean reduced scaled width and mean reduced scaled length) are used for gamma-hadron separation. The gamma-ray energy is estimated from the image intensity taking into account the reconstructed shower geometry, in particular the impact distance. The performance of this analysis method as applied to extended sources can be found in Aharonian et al. (2006).
2. In the 3D model analysis, the Cerenkov light emitted by a shower is modeled in the following way: the photon origins (photosphere) are distributed according to a 3D Gaussian law and their directions are assumed to follow an anisotropic angular distribution, with the overall requirement of rotational symmetry characteristic of an electromagnetic shower. The expected number of Cerenkov photons collected by each phototube of a given telescope is then calculated by integrating the light yield over the corresponding line of sight. A comparison of the observed images to the expected ones by means of a maximum likelihood method allows the rejection of a large fraction of hadronic showers, namely those which are not compatible with rotational symmetry. An additional discrimination between gamma rays and hadrons is provided by the lateral spread of the photosphere (or 3D width) obtained from the likelihood fit. In practice, we use a dimensionless parameter directly related to this quantity, the "reduced 3D width," whose distribution is almost zenith-angle independent. The energy E_0 of the primary gamma ray is then reconstructed calorimetrically from the number of Cerenkov photons obtained from the fit. A complete review of the performance of this analysis method is given in Lemoine-Goumard et al. (2006).

4. MORPHOLOGY

4.1. *Background Subtraction Methods*

For the generation of the excess skymaps for RX J0852.0−4622, two different methods of background subtraction have been applied. The first one is classic: the background level is estimated from OFF-source runs, observing sky regions without any gamma-ray sources in the field of view. For this purpose, 20 hr of OFF runs taken at similar zenith angles are used. All events passing the gamma-ray cuts of the different analysis methods, i.e., gamma-ray–like background events, are used to estimate the background. The second method of background subtraction is more recent and is called the "weighting method" (Lemoine-Goumard & Degrange 2005). In this method, the signal and the background are estimated simultaneously in the same portion of the sky. In each sky bin (treated independently), the signal and the background are estimated from those events originating from this bin exclusively. Each event is characterized by a discriminating parameter, the reduced 3D width defined above. Since its distribution is fairly different for gamma rays and hadrons, the respective numbers in each population are derived by a likelihood fit. Therefore, no cut on the reduced 3D width is necessary. The advantage of these background-subtraction methods is that no assumption on the gamma-ray content in the field of view is necessary. The bin size used in this analysis is 0.05° × 0.05°. The images were further smoothed by a Gaussian distribution with a standard deviation of 0.06° to reduce the statistical fluctuations. This procedure was chosen in order to match the H.E.S.S. angular resolution and the binning of the images. The resulting excess maps are in units of integrated excess counts per Gaussian σ of the smoothing function.

4.2. *Overall Morphology of the Remnant*

In the study of the morphology of an extended source, one of the major objectives is to have the best possible angular resolution. In an array such as H.E.S.S., including four telescopes placed in a square formation, events triggering four telescopes are concentrated in the central region of the array, whereas events triggering two telescopes, being peripheral, are not so accurately reconstructed as the central ones. Therefore, to obtain a high angular resolution (of the order of 0.06°), one can restrict the analysis to events triggering at least three telescopes, which also further reduces the hadronic background. The excess skymap in Figure 1 shows the gamma-ray image of RX J0852.0 4622 in a 4° × 4°

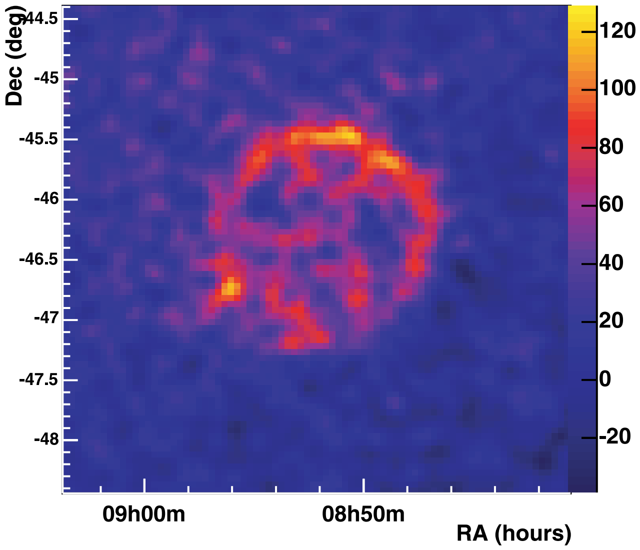

Fig. 1.—Gamma-ray image of RX J0852.0−4622 smoothed by a 0.06° Gaussian. Only events triggering three and four telescopes were accepted in this analysis, leading to a better angular resolution as explained in § 4.2. The linear color scale is in units of excess counts per bin.

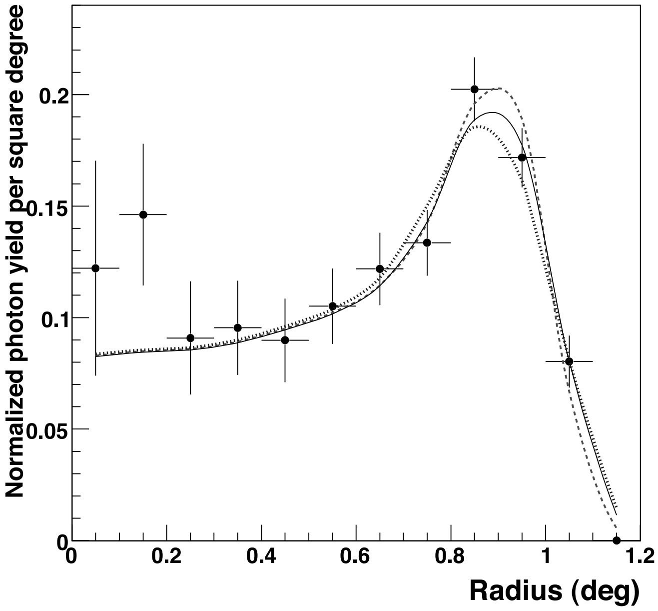

Fig. 2.—Radial profiles around the center of the SNR ($\alpha_{\rm J2000.0} = 8^{\rm h}52^{\rm m}$, $\delta_{\rm J2000.0} = -46°22'$) expected for a shell of varying thickness and uniform emission compared to the H.E.S.S. data (*crosses*) for the northern part of the remnant. The dotted line of the radial profile has been obtained with a thickness of 22.5% of the radius of the remnant, the dashed line with 12.5%, and the solid line with 18.3%. All these histograms have been normalized so that the sum of the contents between 0.3° and 1.2° is equal to unity. [*See the electronic edition of the Journal for a color version of this figure.*]

field of view, obtained with the 3D model and the weighting method by keeping only three- and four-telescope events. The gamma-ray content in this skymap presents a much higher statistics than the one obtained with the H.E.S.S. data set from 2004 February (Aharonian et al. 2005b). The significance is about 19 σ with an excess of ~5200 events, keeping all events inside a radius of 1° around the center of the remnant. In order to explore the robustness of the result, the data set was analyzed using the same calibration and analysis method but applying different sets of cuts, which resulted in different resolutions and statistics, all results being compatible with each other. In addition, the morphology was cross-checked using the standard analysis method for the reconstruction and the ON-OFF method for the background subtraction. The comparison of the results obtained by the two methods in a region of 1.2° radius around the center of the SNR yields a correlation coefficient of 80% ± 1%. These tests show that the gamma-ray morphology of the remnant remains consistent when analyzed with different sets of cuts or with different background subtraction methods.

The morphology appearing from the excess skymap in Figure 1 reveals a very thin shell of 1° radius and ~0.2° thickness. It shows several bright regions in the north, northwestern, and southeastern parts of the SNR. Another feature is the remarkably circular general shape of this shell, even if the southern part shows a more broken (nonuniform) structure than the northern one. This regular morphology very much resembles the image that one would expect from a homogeneously emitting shell. In order to investigate the projection effect of the 3D source into a 2D skymap, a simple geometrical model (“toy model”) of a thin and homogeneous shell has been used and adapted to the data. After calculating the projection, the obtained skymap is smoothed according to the average point-spread function in this data set. The radial profiles (i.e., the number of events per unit solid angle as a function of the distance to the center of the remnant) obtained with the toy model for different values of the shell thickness are then fitted to those obtained from H.E.S.S. data (restricted to three- and four-telescope events) in the northern part of the remnant (declination higher than −46.3°) which exhibits a clear shell as seen on the gamma-ray excess map. For each value of the shell thickness, the only parameter of the fit is the outer radius of the shell. Figure 2 shows that the bright shell observed by H.E.S.S. is well reproduced by the simple geometrical model. In Figure 2, the remarkable point to note is the small value of the shell thickness giving the best fit; it is equal to 18.3% of the radius of the remnant and between 12.5% and 22.5% at 95% confidence level. This contrasts with RX J1713.7−3946, another shell-type SNR resolved by H.E.S.S., in which the shell thickness that best suited the data was about 45% of the radius of the remnant. This good match of the toy model and the H.E.S.S. data clearly shows that the gamma-ray emission detected comes from a thin shell.

4.3. *Energy Dependence of the Morphology*

Figures 3 and 4 show the morphology of RX J0852.0−4622 in two distinct energy bands, $E < 0.5$ TeV and $E > 0.5$ TeV, keeping only events triggering at least three telescopes. The two energy bands were chosen in order to have approximately the same statistics in both data sets. Clearly, the morphology of the remnant is the same in the two energy bands. The overall radial profile in the two energy bands shown in Figure 5 confirms that the morphology does not vary significantly with energy.

5. SPECTRAL ANALYSIS

For the spectral analysis, the source region (ON region) is defined by a circle of 1° radius centered on the position ($\alpha_{\rm J2000.0} = 8^{\rm h}52^{\rm m}$, $\delta_{\rm J2000.0} = -46°22'$). In the study of a point-like source, the restricted selection of events due to the knowledge of the exact gamma-ray origin and the reduced offsets of the source from the center of the camera improve the energy resolution. However, in the present case, these two characteristics are lost, which results in an average energy resolution $\Delta E/E \sim 25\%$ for the 3D model, slightly larger than for a point-like source. The energy resolution can be improved by restricting to three- and four-telescope events at the expense of a smaller statistics (but with the same statistical

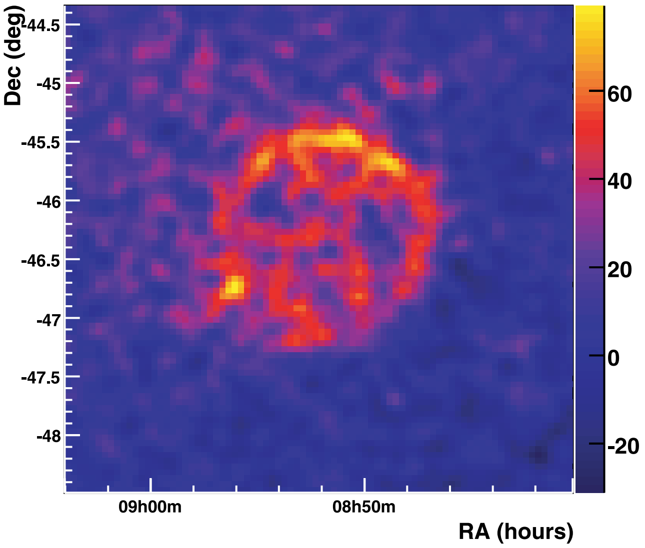

FIG. 3.—Gamma-ray image of RX J0852.0−4622 at energies lower than 0.5 TeV, smoothed by a 0.06° Gaussian. Only events triggering at least three telescopes were kept. The linear color scale is in units of excess counts per bin.

significance). In this study, the two possibilities (restricting to three- and four-telescope events or not) were used in order to verify the stability of our results.

The spectral analysis requires selection criteria that are slightly different from those of the morphological study. Two cuts were applied independently of the telescope multiplicity: a cut on the reduced 3D width and a cut on the image size at 80 photoelectrons. All events passing the cuts and with reconstructed direction within a region of 1° radius from the center of the remnant are considered as ON events.

For the background estimation, OFF events were selected from the same field of view and in the same runs as the ON events by selecting the region symmetric to the ON region with respect to the camera center (“mirrored background”). A minimum distance of 0.1° between the two regions is required in order to avoid any gamma-ray contamination in the OFF data. This approach ensures that background events are taken at the same zenith angle and offset angles as the ON events, which is crucial because of the strong dependence of the effective area on these two quantities.

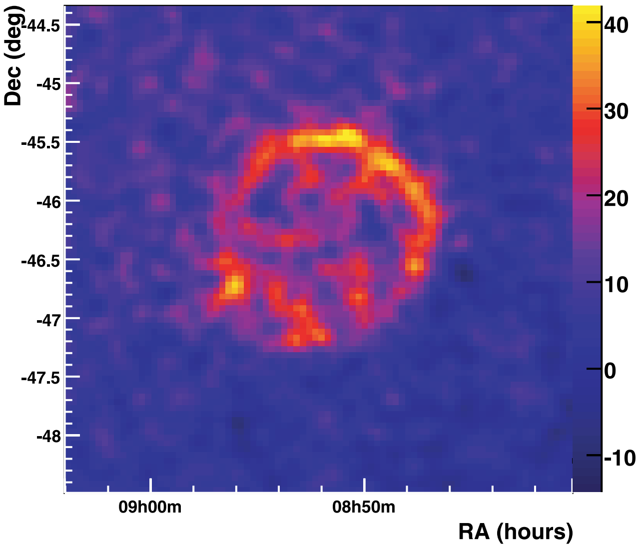

FIG. 4.—Same as Fig. 3 for energies higher than 0.5 TeV.

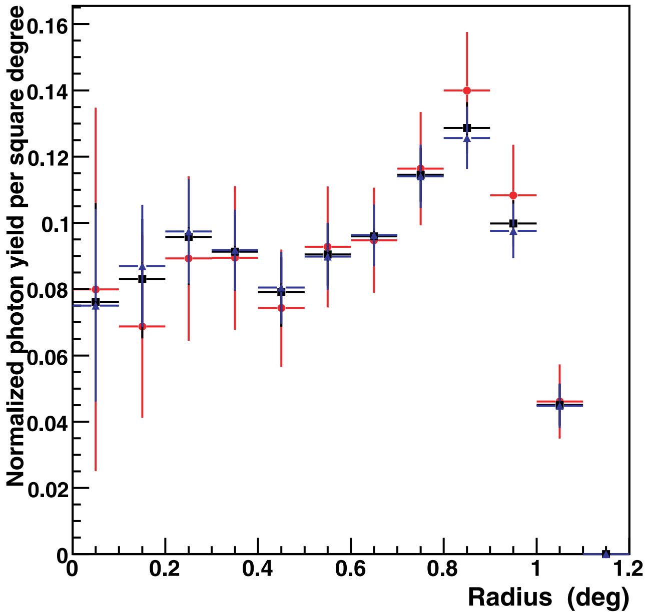

FIG. 5.—Comparison of the radial profiles of the whole remnant in different energy bands. The black squares show the radial profile for all energy events, the circles for energies higher than 0.5 TeV, and the triangles for energies lower than 0.5 TeV. The different distributions have all been normalized to unity to enable a direct comparison.

The energy spectrum of the gamma-ray excess is then obtained by the method of Piron (2000). In this method, an a priori spectral shape is assumed whose parameters are obtained by fitting the expected distribution to the reconstructed energy distribution. In this procedure, gamma-ray acceptances and resolutions calculated from simulations are taken into account.

The differential energy spectrum thus obtained is shown in Figure 6. It extends from 300 GeV up to 20 TeV. The spectral parameters were obtained from a maximum likelihood fit of a power-law hypothesis $dN/dE = N_0(E/1\ \mathrm{TeV})^{-\Gamma}$ to the data, resulting in an integral flux above 1 TeV of $(15.2 \pm 0.7_{\rm stat} \pm 3.20_{\rm syst}) \times 10^{-12}\ \mathrm{cm^{-2}\ s^{-1}}$ and a spectral index of $2.24 \pm 0.04_{\rm stat} \pm 0.15_{\rm syst}$. The present data include many more statistics,

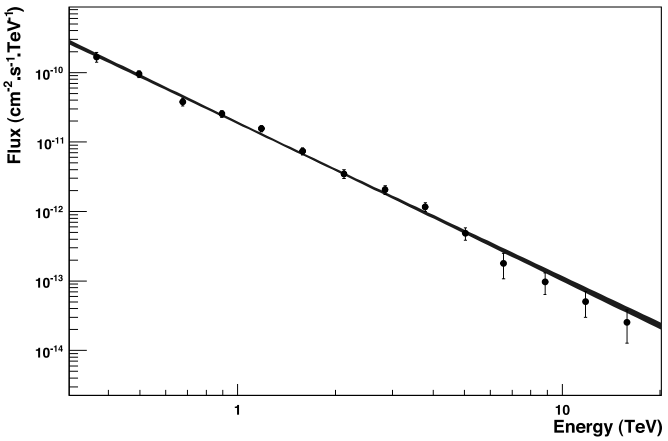

FIG. 6.—Differential energy spectrum of RX J0852.0−4622, for the whole region of the SNR. The shaded area gives the 1 σ confidence region for the spectral shape under the assumption of a power law. The spectrum ranges from 300 GeV to 20 TeV. [*See the electronic edition of the Journal for a color version of this figure.*]

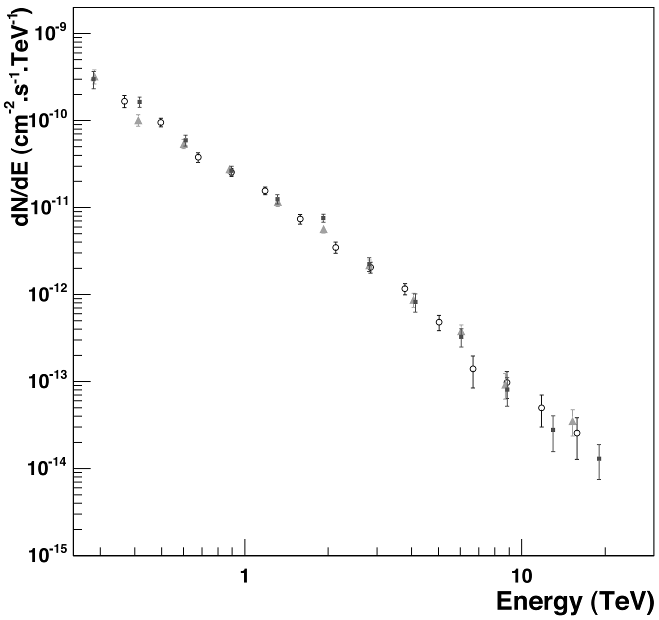

FIG. 7.—Three spectra that were produced to investigate the systematic uncertainties. The open circles show the spectrum obtained with the 3D model analysis and using the reflection of the ON region from the center of the camera to estimate the background. The squares' spectrum was obtained with the standard analysis and the same background estimation, but another spectral analysis technique (Aharonian et al. 2006). The triangles' spectrum was obtained by using the standard analysis and the same spectral analysis technique as the squares' spectrum, but the background estimation was done with OFF runs. [*See the electronic edition of the Journal for a color version of this figure.*]

especially at high energy, than the previous H.E.S.S. measurement (Aharonian et al. 2005b) and a slight deviation from a pure power law can be seen in Figure 6. This can explain the average spectral index being slightly higher than the one from the previous measurement: $2.1 \pm 0.1_{\rm stat} \pm 0.2_{\rm syst}$. To confirm this spectrum, two other estimates of the spectrum of the whole remnant were obtained by using other techniques. These checks ensure that the systematics introduced by the spectral analysis technique or by the background estimation are small. For these tests, the standard analysis method was applied by using a cut on the "scaled parameters" and on the image size at 80 photoelectrons. In Figure 7, two different estimates of the spectrum are superimposed on the one obtained with the 3D model. One was computed by using the same background estimation with a mirror region and the other by using a background estimation based on OFF runs taken at similar zenith angles. All spectra are compatible with each other and all show an indication of deviation from a power law at high energy.

6. RX J0852.0−4622 AT OTHER WAVELENGTHS

6.1. *Analysis of ASCA Data*

ASCA archival data of RX J0852.0−4622 were used to study the nonthermal emission of the remnant in the X-ray band. Figure 8 shows the *ASCA* GIS (GIS2 and 3) mosaic image of RX J0852.0−4622 in the 0.7–10.0 keV energy band (Tsunemi et al. 2000) obtained by using seven distinct pointings (N1–N7) which almost cover the entire remnant. Standard quality criteria (screening procedures) were applied to *ASCA* GIS data, and spectra were extracted from the seven non-overlapping regions shown in Figure 8. Since the soft thermal emission from the Vela SNR foreground is spatially variable, background spectra were produced by using blank sky event files, which are considered to contain both non-X-ray background and cosmic X-ray background, except for the central pointing (N2). For this region, due to different observation conditions, the background spectrum was extracted from Large Sky Survey (LSS) data observed during the *ASCA* PV phase (Ueda et al. 1999). To derive the spectral parameters, the emission was modeled with two components. A thermal model was used to account for the soft thermal emission from the Vela SNR, with a column density fixed at $N_{\rm H} = 10^{20}$ cm^{-2} (Lu & Aschenbach. 2000) and a temperature of kT_e (low) = 0.1 keV, typical values for Vela.[32] An absorbed power law was used for the hard emission. A simultaneous spectral fitting was performed with both GIS instruments from 0.7 up to 7.0 keV. Figure 9 shows the spectrum extracted from region N1 with the best-fit models; it exhibits some line-like features below 2 keV that originates from thermal emission from the Vela SNR and/or RX J0852.0−4622. The

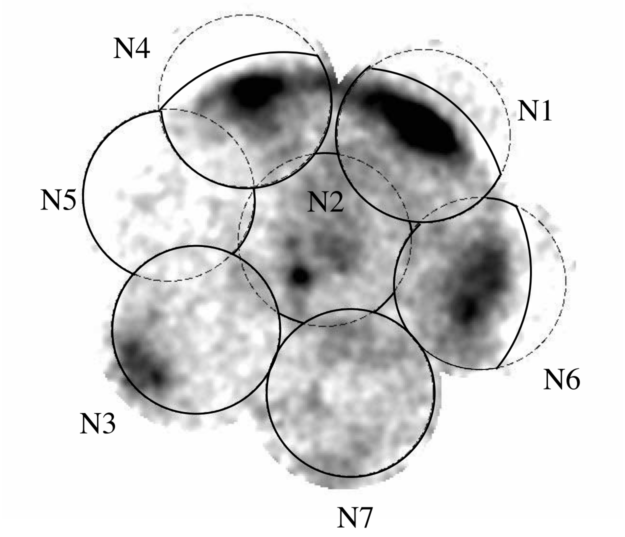

FIG. 8.—*ASCA* GIS mosaic image in the 0.7–10 keV energy band (Tsunemi et al. 2000). The gray scale is logarithmic. The seven regions used for the spectral analysis are denoted by solid lines, while the dashed circles represent the seven pointings.

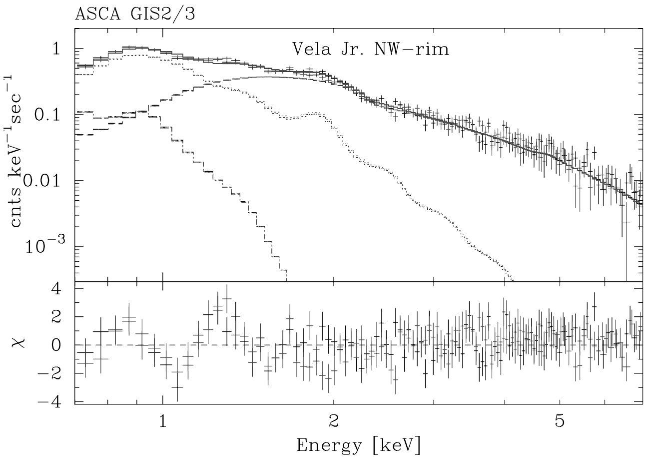

FIG. 9.—*ASCA* GIS (GIS2 and GIS3) spectrum from N1 source region depicted in Fig. 8. The different components of the best-fit models (absorbed power law and both thermal spectra) are indicated by the lower histograms. Residuals are presented in the bottom plot. [*See the electronic edition of the Journal for a color version of this figure.*]

---

[32] One should note that the GIS response is not well suited to determine the soft component which led us to fix the values of kT_e (low) and $N_{\rm H}$ (Vela).

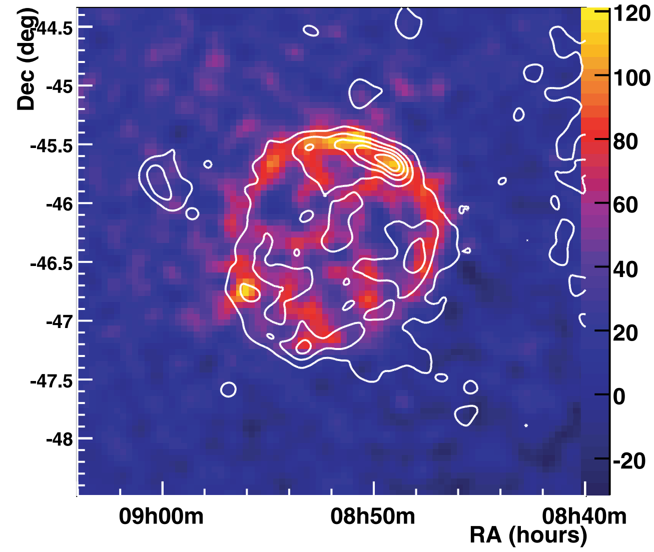

FIG. 10.—Excess skymap of RX J0852.0−4622 smoothed with a Gaussian of 0.06° standard deviation. The white lines are the contours of the X-ray data from the *ROSAT* All Sky Survey for energies higher than 1.3 keV (smoothed with a Gaussian of 0.06° standard deviation to enable direct comparison of the two images). The linear color scale is in units of excess counts per bin.

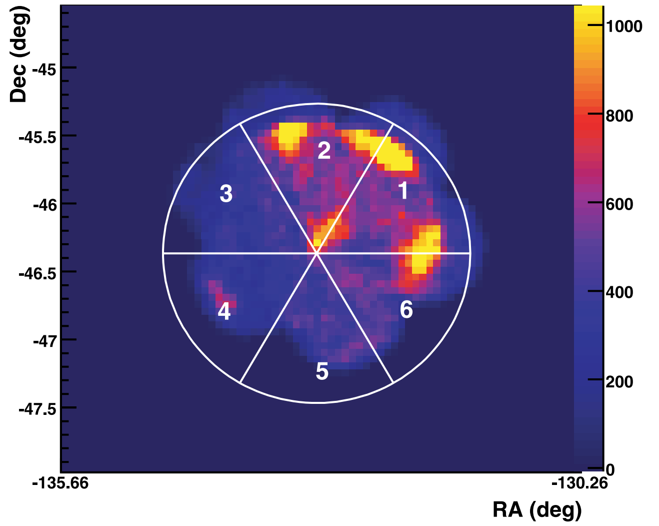

FIG. 11.—*ASCA* X-ray image of RX J0852.0−4622. The six regions used in the radial profiles are indicated. One can notice that the coverage of the remnant is not complete in regions 4, 5, and 6. The linear color scale is in units of excess counts per bin.

resulting spectral parameters of the fit are the photon index, $\Gamma = 2.79 \pm 0.09$, the column density for the nonthermal component, $N_{\rm H} = 6.2^{+1.4}_{-1.3} \times 10^{21}$ cm^{-2}, and the high temperature of the Vela SNR thermal component, kT_e (high) = 0.56 ± 0.1 keV. These values are well consistent with previous results (Slane et al. 2001; Iyudin et al. 2005; Bamba et al. 2005a). The derived nonthermal flux from region N1 in the 2–10 keV energy band is $(1.87 \pm 0.06) \times 10^{-11}$ erg s^{-1} cm^{-2}, while the thermal flux is ~30 times smaller than the nonthermal flux in 2–10 keV band. Some residuals are still visible around 1 keV and suggest that another thermal component, which might originate from RX J0852.0−4622, is needed. For the other six regions, spectra have been fitted with the same procedure as described above. The resultant photon indices are between 2.5 and 2.8 and the total flux for the seven regions is $(8.3 \pm 0.2) \times 10^{-11}$ erg s^{-1} cm^{-2} (2–10 keV). All errors described in this section are statistical and given at 90% confidence level. The systematic error on the flux implied by the procedure has been estimated as follows: the error due to the uncertainty in the instrumental response is ±10% and the one due to the uncertainty on the surface brightness variation in RX J0852.0−4622 is ±20%.

6.2. *Morphological Comparison between H.E.S.S. and X-Rays*

Figure 10 presents the gamma-ray excess map obtained by H.E.S.S. with the superimposed contours of the X-ray data from the *ROSAT* All Sky Survey. The overall gamma-ray morphology seems to be similar to the one seen in the X-ray band, especially in the northern part of the remnant where a brightening is seen in both wave bands. The correlation coefficient between the gamma-ray and the X-ray counts in bins of 0.2° × 0.2° is found to be equal to 0.60 and between 0.54 and 0.67 at 95% confidence level. The use of *ASCA* data gives a similar result. The data of the various instruments were then compared to each other in six different sectors defined in Figure 11. In each region, the radial profiles were determined. A binning of 0.1° for the radial profiles was used; this value, larger than the point-spread function of each instrument, allows the safe comparison of their data. All the radial profiles were normalized to unity. The results of this study are shown in Figure 12. One should note that, due to an incomplete coverage of the SNR in regions 4, 5, and 6, the *ASCA* data are not reliable at distances larger than ~0.7° in these regions, and were thus not included; this incomplete coverage is visible in Figure 11. The different radial profiles are in good agreement with each other in all regions. Differences between X-rays and TeV gamma rays seem to appear mainly in region 3, where a peak is seen only in the TeV regime. Unfortunately, as the *ASCA* data are incomplete and the *ROSAT* data are contaminated by the Vela SNR, a more quantitative conclusion (for example, on the question of the boundaries of the SNR) cannot be drawn.

6.3. *Radio Observations*

Mosaic observations of RX J0852.0−4622 with the Australian Telescope Compact Array (ATCA) were undertaken in 1999 November at frequencies of 1384 and 2496 MHz (Stupar et al. 2005). Figure 13 is a mosaic image of RX J0852.0−4622 obtained from 110 pointings at 1384 MHz. The image suffers from sidelobes originating from the strong radio source CTB 31 (RCW 38). A certain similarity between the H.E.S.S. image (Fig. 1) and the radio image of RX J0852.0−4622 (Fig. 13) can be noticed at first glance. The overall morphology appears to be similar; many features seen in the TeV skymap coincide well with the radio image, such as the bright region in the northern part of the shell and the central filamentary structures inside the SNR. Indeed, a high correlation can be seen when superimposing the radio contours to the H.E.S.S. images, as shown in Figure 14. The ATCA contours directly match the structures from the H.E.S.S. skymap and the features obtained inside the remnant are also well reproduced.

6.4. CO *Observations*

CO data at 2.6 mm wavelength of the region of the Vela Molecular Ridge and its surroundings were taken with the 4 m, millimeter and submillimeter telescope NANTEN in 1999 (Moriguchi et al. 2001). Figure 15 shows the integrated molecular column density derived from CO data, in the RX J0852.0−4622 region. A high density is clearly visible in the eastern part of the remnant (which corresponds to regions 3 and 4 defined in Fig. 11) due to the presence of the Vela Molecular Ridge (VMR). Unfortunately,

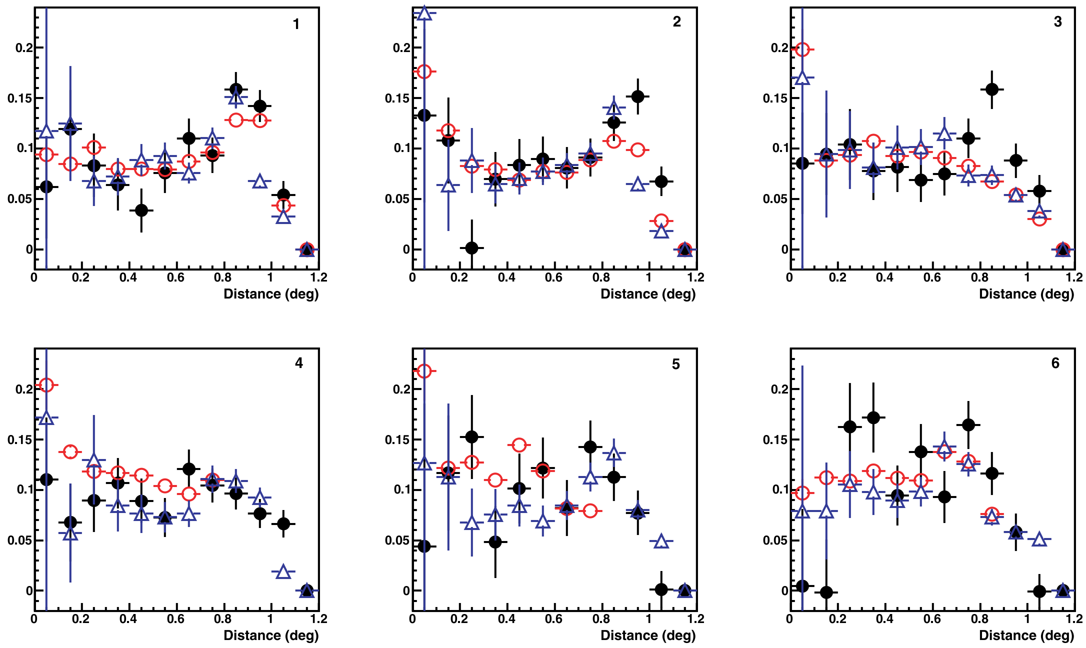

FIG. 12.—Radial profiles for the six regions marked in Fig. 11. The filled circles represent the H.E.S.S. excess counts per unit solid angle as a function of the distance r from the center of the remnant. The open circles represent the radial profiles of the *ASCA* X-ray data. The open triangles represent the radial profiles obtained with the X-ray data from the *ROSAT* All Sky Survey. The different distributions have been normalized to unity in each region to enable a direct comparison. Note that the coverage of the SNR by *ASCA* was not complete in the regions 4, 5, and 6.

in region 4 uncertainties concerning the X-ray data (incomplete coverage and contamination by the Vela SNR foreground) preclude any firm conclusion concerning a possible anticorrelation with the CO data. On the other hand, no clear evidence of interaction between VHE particles and the VMR is seen in the H.E.S.S. data, since the gamma-ray flux does not vary by more than a factor of 2 from the eastern to the western sides, whereas the molecular column density drops by a factor of ~20. Figure 16 shows the correlation coefficient between the CO and the H.E.S.S. data calculated in different intervals of distance varying from −0.2 to 3.2 kpc, in the six regions defined previously. Distances were estimated by using a galactic rotation model (Brand & Blitz 1993). No clear correlation can be seen in this (Fig. 16).

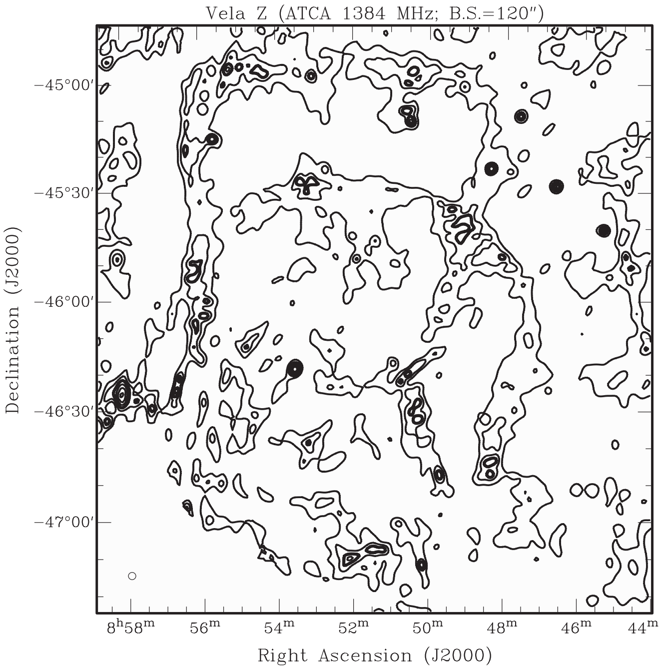

FIG. 13.—ATCA mosaic image of RX J0852.0−4622 at 1384 MHz. Contours are from 0.01 to 0.9 in steps of 0.02 Jy beam^{-1}. The synthesized beam of the mosaic ATCA observations is $120'' \times 120''$. For a better presentation of features inside the remnant, RCW 38 is not shown.

7. CONSTRAINTS ON SOURCE ENERGETICS AND EMISSION MECHANISM

As stated above, the parameters of the SNR RX J0852.0−4622 are not well known, in particular its age and its distance. Indeed, the remnant could be as close as the Vela SNR ($D \approx 200$ pc) and very young, or as far as the VMR ($D \approx 1$ kpc). This leads to a change in the prediction of the X-ray or gamma-ray luminosity by a factor 25 according to the assumed distance. However, beside the distance, other observational characteristics of the remnant provide some helpful constraints.

7.1. *Main Constraints besides the Spectral Analysis*

The analysis of *ASCA* data enabled Slane et al. (2001) to derive a limit on the thermal content of the remnant emission, and therefore a limit on the density n_0 of the thermally emitting material in the remnant. Using the assumption of thermal equilibrium, the limit obtained is $n_0 < 2.9 \times 10^{-2}(D/1\ \mathrm{kpc})^{-1/2} f^{-1/2}\ \mathrm{cm}^{-3}$, where f is the filling factor of a sphere taken as the emitting volume in the region chosen. It should be noted that this limit is restricted to a gas with temperature above 1 keV because of the contribution of the thermal emission from the Vela SNR at lower energies; higher densities of cooler material are thus not excluded. Furthermore, if the shocks are strongly modified by the accelerated particles, the shock heating is substantially reduced and the X-ray data could be consistent with higher densities. Another important piece of information comes from the measured width of the filaments observed by the *Chandra* satellite. If we assume that these filaments are due to the outer shock, their width determines

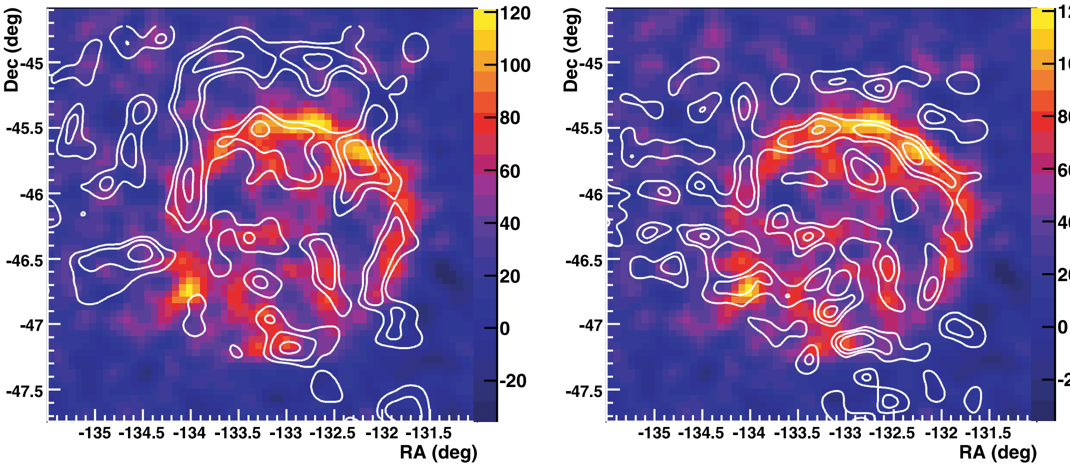

Fig. 14.—Excess skymap of RX J0852.0−4622 smoothed with a Gaussian of 0.06° standard deviation. The white lines are the contours of the ATCA data for a frequency of 1384 MHz on the left and 2496 MHz on the right (smoothed with a Gaussian of 0.06° standard deviation to enable direct comparison of the two images). The linear color scale is in units of excess counts per bin.

the downstream magnetic field B_d. The thickness of the filament observed by *Chandra* in the 2–10 keV energy band is: $w_d = 0.24^{+0.19}_{-0.07}(D/1\ \mathrm{kpc})$ pc. This led Bamba et al. (2005a) to suggest a value of $B_d \sim 500\ \mu$G for a distance of 300 pc. The field evaluation based on the work of Berezhko & Völk (2004) gives values $B_d \sim 350\ \mu$G. Such values imply that the magnetic field is highly amplified. Finally, the morphological analysis of the H.E.S.S. data sets an upper limit on the thickness of the shell $\Delta R < 22.5\%$ of the radius of the SNR. For electrons, which rapidly lose their energy by synchrotron and IC radiation, the escape time out of the shell into the remnant interior (by diffusion and convection) should be larger than the characteristic time of energy losses. Otherwise, their interactions with photons from the cosmic microwave background would lead to a gamma-ray emission region more extended than that observed by H.E.S.S. For protons, for which the timescale for energy losses is longer, the escape time must be larger than the age of the SNR. The characteristic escape time of particles is calculated with the formula $t_{\rm esc} = (t_{\rm diff}^{-1} + t_{\rm conv}^{-1})^{-1}$, $t_{\rm diff}$ being the diffusive escape time in the Bohm diffusion regime and $t_{\rm conv}$ the convective escape time. The diffusive escape time is given by $t_{\rm diff} = \Delta R^2/2D_{\rm diff}$ with $D_{\rm diff}$ the diffusion coefficient for 100 TeV particles and ΔR the upper limit on the width of the shell as resolved by H.E.S.S.; the convective escape time is given by $t_{\rm conv} = 4\Delta R/V_{\rm shock}$ with $V_{\rm shock}/4$ the flow velocity into the interior in the shock frame, as derived from Truelove & McKee (1999) and reported in Table 1. This allows us to calculate a lower limit on the magnetic field $B_{\rm esc}$, reported in Table 1, in order to confine particles of 100 TeV within the thin shell resolved by H.E.S.S. However, it should be noted that the shell thickness in the case of a proton model also reflects the thickness of the gas target and is not necessarily a good indicator of thickness of the zone filled by accelerated particles (unlike the electron case where the cosmic microwave background radiation provides a uniform target). Nevertheless, the condition that the acceleration timescale associated with 100 TeV particles be less than the age of the remnant, or the equivalent condition that the associated diffusion length scales be small compared to the shock radius, lead, within factors of order unity, to identical lower limits on the magnetic field strength.

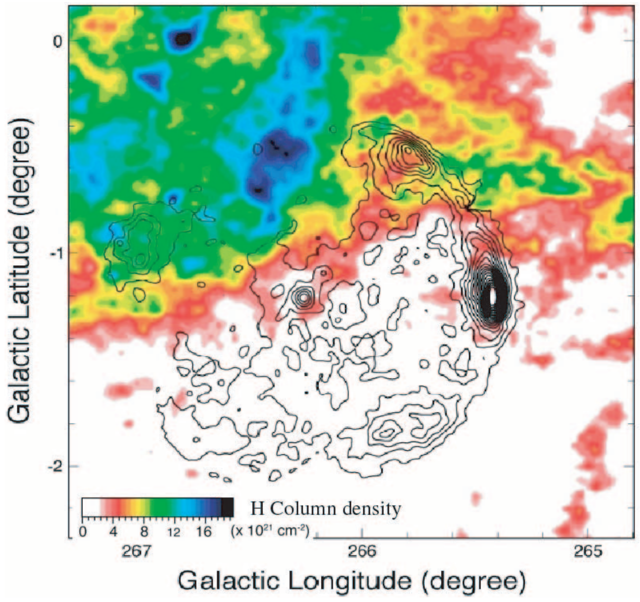

Fig. 15.—Integrated molecular column density, in linear color scale. Overlaid are the contours of the *ASCA* X-ray excess image. Note that the image is shown in Galactic coordinates.

7.2. *Spectral Constraints and Modeling of Emission Processes*

Another constraint comes from the broadband spectral energy distribution (from radio to gamma rays) as interpreted by a model of emission processes taking place in the SNR. The objective is to constrain parameters like the magnetic field, the density of the medium, and the injection spectrum of the primary particles, thanks to a multiwavelength study.

7.2.1. *The Multiwavelength Data*

The gamma-ray spectrum obtained by analyzing the H.E.S.S. data is well described by a power law with a photon index of $2.24 \pm 0.04_{\rm stat} \pm 0.15_{\rm syst}$:

$$\phi(E) = \frac{dN}{dE} = (1.90 \pm 0.08_{\rm stat} \pm 0.40_{\rm syst}) \times 10^{-11}\ \mathrm{cm^{-2}\ s^{-1}\ TeV} \left(\frac{E}{1\ \mathrm{TeV}}\right)^{-2.24 \pm 0.04 \pm 0.15}.$$

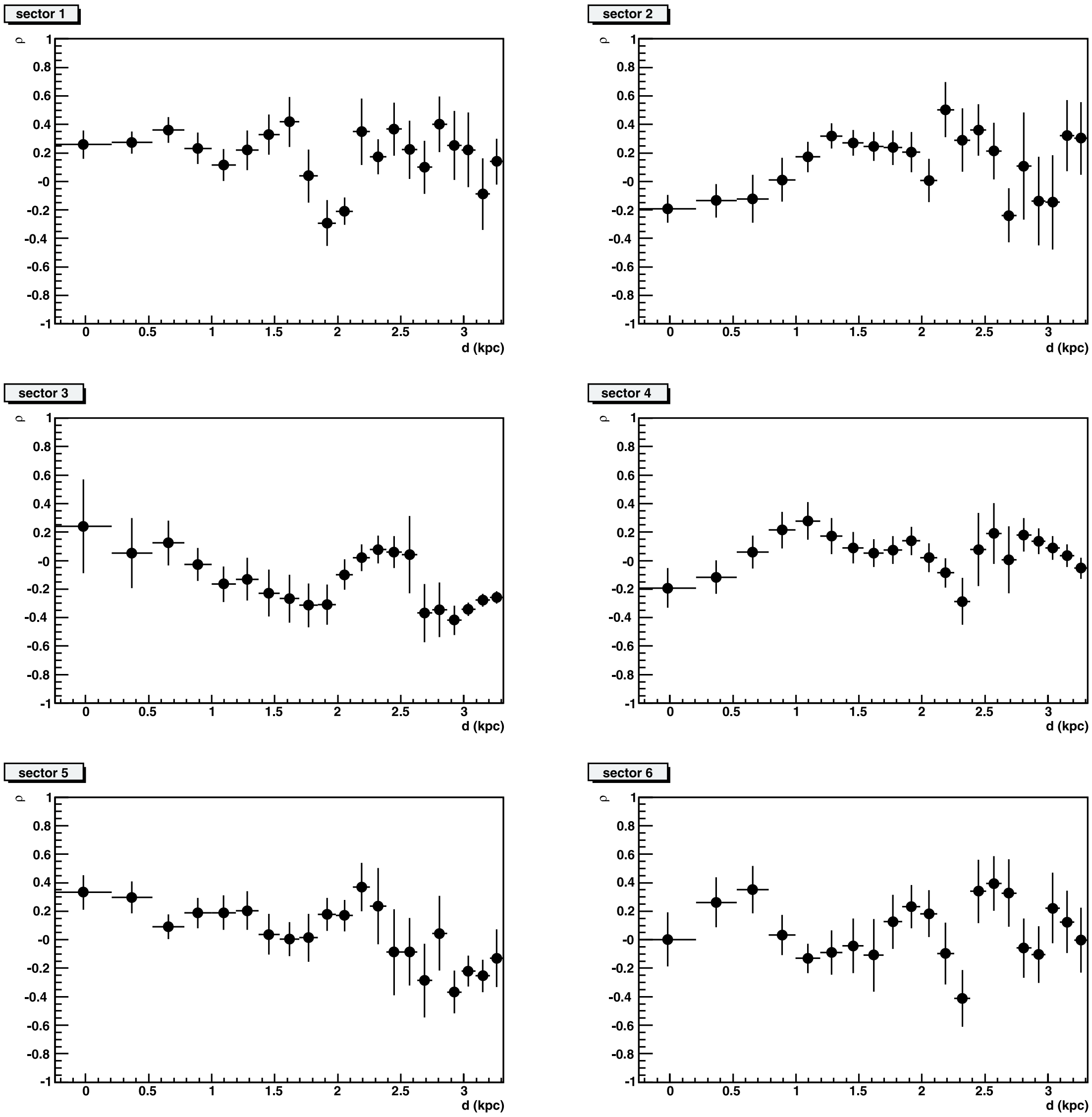

FIG. 16.—Correlation coefficient between the CO intensity and the H.E.S.S. data in different distance intervals for each region defined in Fig. 11. No clear correlation appears in any of the regions analyzed.

This flux can be translated into a global energy flux ω_γ between 1 and 10 TeV by using the formula

$$\omega_\gamma(1\text{–}10\ \text{TeV}) = \int_{1\ \text{TeV}}^{10\ \text{TeV}} E\phi(E)dE = 5.4\times10^{-11}\ \text{erg cm}^{-2}\ \text{s}^{-1},$$

which corresponds to a gamma-ray luminosity $L_\gamma = 2.6\times10^{32}(D/200\ \text{pc})^2$ erg s^{-1}. If one assumes that the gamma-ray flux is entirely due to proton-proton interactions, we can estimate the total energy W_p of accelerated protons in the range 10–100 TeV required to produce this gamma-ray luminosity. In this energy range, the characteristic cooling time of protons through the π^0 production channel is approximately independent of the energy and can be estimated by (Aharonian et al. 2004b) $\tau_\gamma = 4.4\times10^{15}(n/1\ \text{cm}^{-3})^{-1}$ s. Thus,

$$W_p(10\text{–}100\ \text{TeV}) \approx L_\gamma\tau_\gamma \approx 1.1\times10^{48}\left(\frac{D}{200\ \text{pc}}\right)^2\left(\frac{n}{1\ \text{cm}^{-3}}\right)^{-1}\text{erg}.$$

Assuming that the proton spectrum continues down to $E\approx1$ GeV with the same spectral slope as that of the photon spectrum, the total energy injected into protons is estimated to be

$$W_p^{\text{tot}} \approx 10^{49}\left(\frac{D}{200\ \text{pc}}\right)^2\left(\frac{n}{1\ \text{cm}^{-3}}\right)^{-1}\text{erg}.$$

Values of W_p^{tot} are reported in Table 1 for different distances and densities of the ambient medium.

The X-ray spectral analysis of the whole remnant in the 2–10 keV energy band was presented in § 6.1: the nonthermal spectrum is well described by a power law with a spectral index of 2.65 ± 0.15 and a flux $F_{\text{X}} = (8.3\pm0.2)\times10^{-11}$ erg cm^{-2} s^{-1}. The fluxes at 1.40 and 2.42 GHz were taken from the analysis of the Parkes data by Duncan & Green (2000). Later on, we shall use these multiwavelength measurements when comparing the H.E.S.S. spectral data to broadband models.

7.2.2. *Modeling the Emission Processes*

In the simple model used here, we assume that primary particles (protons and electrons) are injected at a constant rate with

TABLE 1

Magnetic Field, Total Energy of Accelerated Protons, Efficiency, and Age of the Supernova Remnant for Different Values of Distance, Density of the Medium, and Ejected Mass

D (pc)	n (cm^{-3})	$M_{\rm ej}$ ($M_\odot$)	$V_{\rm shock}$ (km s^{-1})	$B_{\rm esc}$ (μG)	$W_p^{\rm tot}$ (10^{49} erg)	Efficiency (%)	Age (yr)
200.............	0.1	1.4	6670	29.0	10	10	293
		14	3751	51.6	10	10	521
200.............	0.01	1.4	11862	16.3	100	100	165
		14	6670	29.0	100	100	293
600.............	0.1	1.4	2032	18.5	90	90	2292
		14	1645	39.2	90	90	3565
600.............	0.01	1.4	5203	12.4	900	900	1127
		14	2926	22.0	900	900	2004
1000...........	0.1	1.4	945	20.1	250	250	7531
		14	944	34.5	250	250	9080
1000...........	0.01	1.4	2988	9.3	2500	2500	2871
		14	1994	19.4	2500	2500	4900

Notes.—Magnetic field $B_{\rm esc}$, total energy of accelerated protons $W_p^{\rm tot}$, efficiency and age of the SNR (assuming an energy explosion of 10^{51} erg) for different values of distance D, density of the medium n and ejected mass $M_{\rm ej}$. For the latter, we have chosen two possible values for RX J0852.0−4622: 1.4 $M_\odot$, which is typical for SNIa and 14 $M_\odot$ as an average value for SNII. $B_{\rm esc}$ is the lower limit on the magnetic field allowing the confinement particles of 100 TeV in the thin shell resolved by H.E.S.S. It has been calculated from the value of the shock velocity $V_{\rm shock}$ indicated in this table as derived from Truelove & McKee (1999).

the same spectral shape, namely a power law with an exponential cutoff at the energy E_0, into a spherical shell of fixed thickness ΔR. As seen previously, the H.E.S.S. data require $\Delta R < 22.5\%$ of the remnant radius. The injection is supposed to last a time T (the age of the SNR) in a region of magnetic field B and ambient density n. The electron to proton ratio $K_{\rm ep}$ is a free parameter. The energy distribution of the electrons is calculated at a fixed time t by taking into account energy losses due to synchrotron radiation, IC scattering, and bremsstrahlung, while the proton spectrum is calculated by taking into account the escape out of the shell by diffusion (in the Bohm diffusion regime) and convection, as described in § 7.1. Adiabatic losses are neglected. The broadband spectrum of the source is then derived by taking into account *p-p* interactions, synchrotron radiation (of primary and of secondary electrons produced via *p-p* interactions), IC scattering, and bremsstrahlung. Concerning the energy density of the target photons in the IC process, we added the contribution of the cosmic microwave background, 0.25 eV cm^{-3}, and that of the Galactic seed photons, namely on average: 0.5 eV cm^{-3} for the optical starlight and 0.05 eV cm^{-3} for the infrared background (Mathis et al. 1983).

It is clear that such a model oversimplifies the acceleration process in an expanding remnant, as discussed by, e.g., Drury et al. (1989) and Berezhko et al. (1996). To this must be added the uncertainties introduced by the dynamics of the ejecta, the nonuniform structure of the ambient medium, and the complexities of the reaction of the accelerated particles on both the magnetic field and the remnant dynamics. However, as a starting point for estimates such a simple model is still, we feel, useful, at least for those cases where the remnant evolution is relatively smooth and the emission is not dominated by relic particles injected and accelerated at earlier times (Yamazaki et al. 2007).

In this study, we explored two different cases of distance (200 pc and 1 kpc), both for the electronic process (gamma rays mainly produced by IC scattering) and for the hadronic process (gamma rays mainly produced by *p-p* interactions). Using the free expansion and Sedov-Taylor phase equations (Truelove & McKee 1999), one can easily find that, in the nearby case, the SNR should be very young (∼500 yr). On the contrary, in the distant case, the SNR would be rather old (∼5000 yr). In the following scenarios, the total energy injected into the protons is fixed to 10^{50} erg (i.e., 10% of the energy of explosion of an average supernova), and the width of the shell must be smaller than 22.5% of the radius of the remnant. The age of the remnant is assumed to be 500 yr at 200 pc and 5000 yr at 1 kpc. The other parameters, namely the characteristics of the injection spectrum (spectral index and cutoff energy), the electron/proton ratio $K_{\rm ep}$ at the injection level, the density of the medium, and the magnetic field are free parameters in the fit.

8. THE ELECTRONIC SCENARIO

If the TeV emission is mainly due to IC scattering, one should note that, independently of the distance assumed, the ratio of the X-ray flux and the gamma-ray flux determines the value of the magnetic field B. In the case of RX J0852.0−4622, assuming that IC emitting electrons are contained in a volume equal to the one responsible for synchrotron emission, one can easily deduce that the magnetic field has to be close to 6 μG.

8.1. *The Case of a Nearby Supernova Remnant* (D = 200 pc)

Figure 17 (*left*) shows the best fit obtained, together with the measurements at different wavelengths: the injection spectrum follows a power law of index 2.4 and an exponential cutoff at 40 TeV; the value of the magnetic field is 6 μG and the density of the medium should be lower than 0.1 cm^{-3} so that the gamma-ray flux produced by *p-p* interactions should not be significant. One can clearly notice that the radio flux predicted by our model is about 3 times larger than the one observed in the radio range by Parkes. Even more constraining is the thickness of the shell observed in gamma rays, which is inconsistent with the observations. Indeed, at 200 pc, our limit on the width of the shell implies $\Delta R < 0.78$ pc, which leads to an escape time by diffusion and convection of about 300 yr for an ambient density of 0.1 cm^{-3} and an energy of 40 TeV. This value is lower than the age of the remnant (∼500 yr), but also lower than the synchrotron loss time of 8700 yr. Electrons above ∼20 TeV will escape the shell and thus automatically produce gamma rays by IC scattering on the cosmic microwave background. These gamma rays have, on average, an energy E_γ greater than 500 GeV. Therefore, we expect to observe a much thicker shell for $E_\gamma \geq 500$ GeV. The present analysis of H.E.S.S. data does not show any variation of the morphology of the remnant with the energy, which highly disfavors this scenario.

8.2. *The Case of a Distant Supernova Remnant* (D = 1 kpc)

In the case of a distant object, the magnetic field must also be close to 6 μG; the only difference comes from the fact that energy losses are no more negligible since the SNR is older (∼5000 yr). These energy losses tend to steepen the electron spectrum, and in order to compensate for this effect the cutoff energy has to be increased in comparison to the preceding case. The parameters of our best fit are an injection spectrum following a power law with an index of 2.4, a cutoff energy of 80 TeV, and an electron/proton ratio $K_{ep} = 3.5 \times 10^{-2}$ (Fig. 17, *right*). The different multiwavelength data are reasonably reproduced despite a radio flux three times larger than the observational data from Parkes. This last point is not critical since the fit could be improved by including nonlinear acceleration effects, which are expected to lead to a steeper rise of the synchrotron SED with frequency above the radio range. In this case, the characteristic time of synchrotron losses is 3700 yr for the maximal energy 80 TeV, while the age of

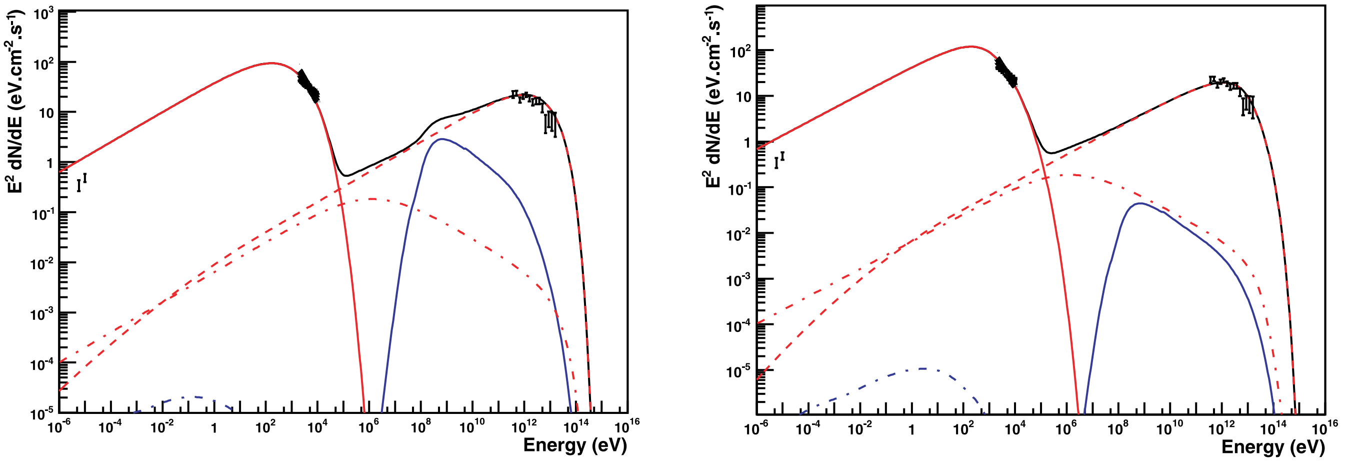

Fig. 17.—Broadband SED models of RX J0852.0−4622 for an electronic scenario in the nearby (*left*) and distant (*right*) case. *Left*: Modeling was done by using an injection spectrum in the form of a power law with an index of 2.4, an exponential cutoff at 40 TeV, and an electron/proton ratio $K_{ep} = 1.7 \times 10^{-3}$. The magnetic field amounts to 6 μG and the density of the ambient medium is 0.008 cm^{-3}. *Right*: Modeling was done by using an injection spectrum in the form of a power law with an index of 2.4, an exponential cutoff at 80 TeV and an electron/proton ratio 3.5×10^{-2}. The magnetic field amounts to 6.5 μG, and the density of the ambient medium is 0.01 cm^{-3}. The Parkes data (Duncan & Green 2000) in the radio range, the *ASCA* data, and the H.E.S.S. data are indicated. Red lines correspond to electrons, and blue lines to protons. The following processes have been taken into account: synchrotron radiation of primary (*solid red lines*) and secondary (*dotted blue lines*) electrons, IC scattering (*dotted red lines*), bremsstrahlung (*dot-dashed red lines*) and proton-proton interaction (*solid blue lines*).

the SNR varies from 4000 to 9000 yr depending on the density of the medium in which it evolves. One can easily find that the escape time is either larger than the synchrotron loss time or larger than the age of the remnant, and is thus irrelevant in this case.

9. THE HADRONIC SCENARIO

First, one can see from Table 1 that the only way to explain the entire gamma-ray flux by proton-proton interactions in a homogeneous medium is to assume that RX J0852.0−4622 is a nearby SNR ($D \leq 600$ pc). Indeed, for larger distances and a typical energy of the supernova explosion, the acceleration efficiency would be excessive (assuming a uniform ambient density compatible with the limit implied by the nondetection of thermal X-rays). Nevertheless, a distance of 1 kpc should also be considered if RX J0852.0−4622 is assumed to be the result of a core collapse supernova which exploded inside a bubble created by the wind of a massive progenitor star, as proposed by Berezhko & Völk (2006) for the SNR RX J1713.7−3946. According to stellar wind theory (Chevalier & Liang 1989), the size of the bubble evolves according to the formula $R = 45(n_0/1\ \mathrm{cm}^{-3})^{-0.2}$ pc. For a density of 1 cm^{-3}, the radius of this bubble would be equal to 45 pc. In the case of a nearby SNR, its size would be significantly lower than the size of the bubble and the hypothesis of a homogeneous medium would be satisfactory. On the opposite, for larger distances ($D \sim 1$ kpc), the presence of the VMR can produce a sudden increase of the density leading to a smaller bubble (15.6 pc for a density of 200 cm^{-3}), which would make the proton-proton interactions efficient at the outer shock. In any case, independently of the distance of the remnant, the extension of the H.E.S.S. spectrum up to 20 TeV implies an energy cutoff E_0 higher than 100 TeV. If we assume that energy losses are negligible over the lifetime of the remnant, the synchrotron spectrum can then be approximated by the formula (Reynolds 1998)

$$F(E) \propto E^{-(\Gamma+1)/2} \exp\left[-(E/E_m)^{1/2}\right],$$

with

$$E_m \approx 0.02(B/10\ \mu\mathrm{G})(E_0/10\ \mathrm{TeV})^2\ \mathrm{keV}.$$

This relation implies that the magnetic field should be lower than 10 μG to obtain a synchrotron peak centered at an energy lower than 2 keV. The gamma-ray flux would then be entirely produced by IC scattering (as seen previously in the electronic process) which enables us to exclude this situation. Therefore, the magnetic field should be high enough to produce significant energy losses during the lifetime of the remnant t_0 (∼500 yr) and create a break in the synchrotron spectrum. Referring to Aharonian et al. (1997), to obtain a break at an energy E_b close to ∼0.2 keV, one would need a magnetic field higher than 40 μG:

$$E_b = 2.9\left(\frac{B}{10\ \mu\mathrm{G}}\right)^{-3}\left(\frac{t_0}{10^3\ \mathrm{yr}}\right)^{-2}\ \mathrm{keV}.$$

9.1. *The Case of a Nearby supernova Remnant* (D = 200 pc)

In this case, our best fit is obtained for an injection spectrum in the form of a power law with an index of 2.1, a cutoff at 110 TeV, and a very low electron/proton ratio of $K_{ep} = 2.4 \times 10^{-6}$. The density of the medium is 0.2 cm^{-3} and the magnetic field amounts to 120 μG; these two values are compatible with both the limit implied by the absence of thermal X-rays and the thin filaments resolved by *Chandra*. On the other hand, one can note in Figure 18 (*left*) that such a model with the above parameters does not provide a good description of the *ASCA* data, since the energy losses tend to steepen the electron spectrum. However, knowing the difficulty of the X-ray spectral analysis, this point cannot be used to exclude this scenario. Furthermore, a better agreement could be obtained by simply relaxing the assumption used in the model that electrons and protons have similar injection spectra.

9.2. *The Case of a Distant Supernova Remnant* (D = 1 kpc)

In this last case, if the density were low enough to be compatible with the absence of thermal X-rays, Table 1 shows that the values of W_p^{tot} required to account for the total observed gamma-ray flux exceed the total energy of the supernova explosion assumed in the present calculation or would require an anomalously energetic explosion. As stated previously, a way out of this difficulty would be to consider the case of a bubble created by the

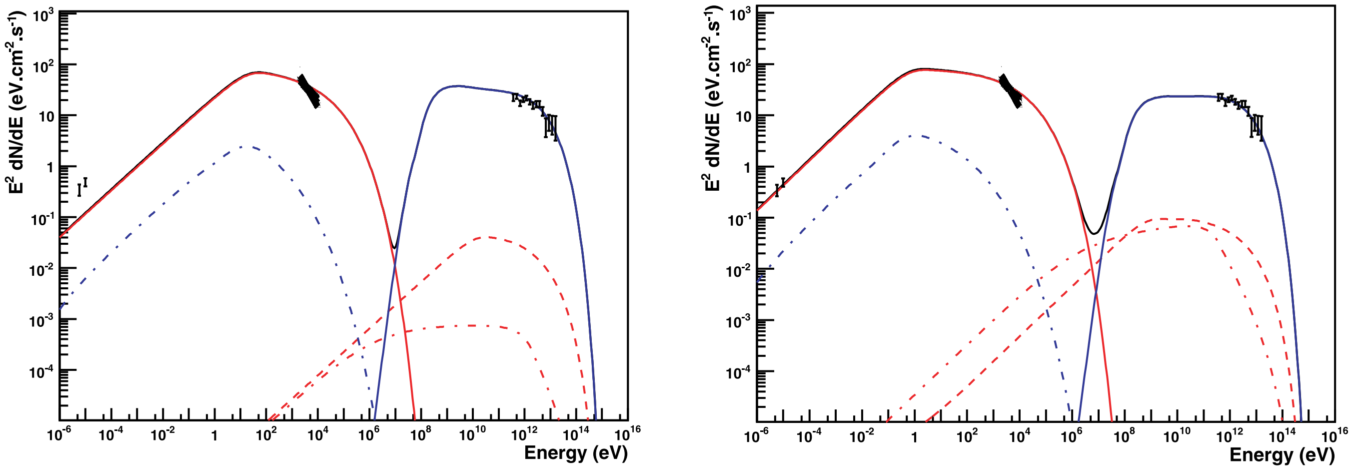

FIG. 18.—Broadband SED models of RX J0852.0−4622 for a hadronic scenario in the nearby (*left*) and distant (*right*) case. *Left*: Modeling was done by using an injection spectrum in the form of a power law with an index of 2.1, an exponential cutoff at 110 TeV and an electron/proton ratio 2.4×10^{-6}. The magnetic field amounts to 120 μG, and the density of the ambient medium is 0.20 cm^{-3}. *Right*: Modeling was done by using an injection spectrum in the form of a power law with an index of 2.0, an exponential cutoff at 100 TeV and an electron/proton ratio 4.5×10^{-4}. The magnetic field amounts to 85 μG, and the density of the ambient medium is 2.0 cm^{-3}. The Parkes data (Duncan & Green 2000) in the radio range, the *ASCA* data, and the H.E.S.S. data are indicated. Red lines correspond to the electrons, and blue lines to protons. The following processes have been taken into account: synchrotron radiation of primary (*solid red lines*) and secondary (*dotted blue lines*) electrons, IC scattering (*dotted red lines*), bremsstrahlung (*dot-dashed red lines*) and proton-proton interaction (*solid blue lines*).

wind of the massive progenitor. Actually, our best fit is obtained for an injection spectrum in the form of a power law with an index $\Gamma = 2.0$, a cutoff energy at $E_0 = 100$ TeV, and an electron/proton ratio of 4.5×10^{-4} (Fig. 18, *right*). The density of the medium is found to be 2.0 cm^{-3}, which is acceptable in the framework of the bubble scenario. The magnetic field, 85 μG, is compatible with the very thin shell resolved by H.E.S.S. Finally, one should note that our model perfectly reproduces the radio and the H.E.S.S. data, but only approximately the slope coming from the *ASCA* spectral analysis.

10. CONCLUSIONS

We have firmly established that the shell-type supernova remnant RX J0852.0−4622 is a TeV emitter and for the first time we have resolved its morphology in the gamma-ray range. The thin shell observed by H.E.S.S. is highly correlated with the emission observed in X-rays with the *ROSAT* All Sky Survey and *ASCA*, but is also very similar to the morphology resolved in radio by ATCA. The overall gamma-ray energy spectrum extends over 2 orders of magnitude, providing direct proof that particles of ~100 TeV are accelerated at the shock. There is an indication of deviation from a pure power law at high energy, but the lack of statistics does not enable us to draw any firm conclusions on this point. This spectrum is very similar to that of the other shell-type supernova remnant resolved by H.E.S.S., RX J1713.7−3946, although the morphology of the latter was very different with a much thicker shell.

The question of the nature of the particles producing the gamma-ray signal observed by H.E.S.S. was also addressed. Despite the large uncertainty concerning the parameters of RX J0852.0−4622, the H.E.S.S. data already give some strong constraints. In the case of a close by remnant, the results of the morphological study combined with our spectral modeling highly disfavor the electronic scenario which is unable to reproduce the thin shell observed by H.E.S.S. and the thin filaments resolved by *Chandra*. The hadronic scenario can approximately reproduce the data at the expense of a very low electron/proton ratio. In the case of a medium distance, the explosion energy needed to explain the gamma-ray flux observed by H.E.S.S., taking into account the limit on the density implied by the absence of thermal X-rays, would disfavor the hadronic process. At larger distances, both the electronic and the hadronic scenario are possible at the expense, for the electronic process, of a low magnetic field of ≈6 μG. Such a small magnetic field exceeds typical interstellar values only slightly, and is difficult to reconcile with the theory of magnetic field amplification at the region of the shock (Bell & Lucek 2001).

Finally, it appears clearly from Figures 17 and 18 that the flux expected for lower energy gamma rays ($E < 200$ GeV) for the electronic process (synchrotron + IC scattering) or for the hadronic process (proton-proton interactions) are significantly different. The results which should hopefully be obtained by *INTEGRAL*, *GLAST*, or H.E.S.S. II will therefore have a great interest for the domain.

The support of the Namibian authorities and of the University of Namibia in facilitating the construction and operation of H.E.S.S. is gratefully acknowledged, as is the support by the German Ministry for Education and Research (BMBF), the Max Planck Society, the French Ministry for Research, the CNRS-IN2P3, and the Astroparticle Interdisciplinary Programme of the CNRS, the UK Particle Physics and Astronomy Research Council (PPARC), the IPNP of the Charles University, the South African Department of Science and Technology and National Research Foundation, and by the University of Namibia. We appreciate the excellent work of the technical support staff in Berlin, Durham, Hamburg, Heidelberg, Palaiseau, Paris, Saclay, and in Namibia in the construction and operation of the equipment. M. Filipovic would like to thank Milorad Stupar for his work on the ATCA data.

REFERENCES

Aharonian, F., et al. (the H.E.S.S. Collaboration). 2004a, Astropart. Phys., 22, 109

———. 2005a, A&A, 430, 865

———. 2005b, A&A, 437, L7

———. 2006, A&A, 449, 223

Aharonian, F. A. 2004b, in Very High Energy Cosmic Gamma Radiation (River Edge: World Scientific)

Aharonian, F. A., Atoyan, A. M., & Kifune, T. 1997, MNRAS, 291, 162

Aharonian, F. A., et al. (the H.E.S.S. Collaboration). 2004c, Nature, 432, 75

Aschenbach, B. 1998, Nature, 396, 141

Aschenbach, B., Iyudin, A. F., & Schönfelder, V. 1999, A&A, 350, 997

Bamba, A., Yamazaki, R., & Hiraga, J. S. 2005a, ApJ, 632, 294

Bamba, A., et al. 2005b, ApJ, 621, 793

Bell, A. R., & Lucek, S. G. 2001, MNRAS, 321, 433

Berezhko, E. G., Elshin, V. K., & Ksenofontov, L. T., 1996, J. Exp. Theor. Phys., 82, 1

Berezhko, E. G., & Völk, H. J. 2004, A&A, 419, L27

———. 2006, A&A, 451, 981

Bernlöhr, K., et al. 2003, Astropart. Phys., 20, 111

Brand, J., & Blitz, L. 1993, A&A, 275, 67

Chen, W., & Gehrels, N. 1999, ApJ, 514, L103

Chevalier, R. A., & Liang, E. P. 1989, ApJ, 344, 332

Combi, J. A., Romero, J. E., & Benaglia, P. 1999, ApJ, 519, L177

de Naurois, M., et al. 2005, in Proc. Towards a Network of Atmospheric Cherenkov Detectors VII, ed. B. Degrange & G. Fontaine (Palaiseau: Ecole Polytechnique), 149

Duncan, A. R., & Green, D. A. 2000, A&A, 364, 732

Drury, L. O'C., Aharonian, F. A., & Völk, H. 1994, A&A, 287, 959

Drury, L. O'C., Markiewicz, W. J., & Völk, H. J. 1989, A&A, 225, 179

Enomoto, R., et al. 2002, Nature, 416, 823

Funk, S., et al. 2004, Astropart. Phys., 22, 285

Hashimoto, T., et al. 2001, Nucl. Phys. A, 686, 591

Hinton, J. A. 2004, NewA Rev., 48, 331

Iyudin, A. F., et al. 1998, Nature, 326, 142

———. 2005, A&A, 429, 225

Kargaltsev, O., et al. 2002, ApJ, 580, 1060

Katagiri, H., et al. 2005, ApJ, 619, L163

Koyama, K., et al. 1995, Nature, 378, 255

———. 1997, PASJ, 49, L7

Lemoine-Goumard, M., & Degrange, B. 2005, in Proc. Towards a Network of Atmospheric Cherenkov Detectors VII, ed. B. Degrange & G. Fontaine (Palaiseau: Ecole Polytechnique), 209

Lemoine-Goumard, M., Degrange, B., & Tluczykont, M. 2006, Astropart. Phys., 25, 195

Lemoine-Goumard, M., et al. 2005, in Proc. Towards a Network of Atmospheric Cherenkov Detectors VII, ed. B. Degrange & G. Fontaine (Palaiseau: Ecole Polytechnique), 173

Lu, F. J., & Aschenbach, B. 2000, A&A, 362, 1083

Mathis, J. S., Mezger, P. G., & Panagia, N. 1983, A&A, 128, 212

Mereghetti, S. 2001, ApJ, 548, L213

Moriguchi, Y., et al. 2001, PASJ, 53, 1025

Muraishi, H., et al. 2000, A&A, 354, L57

Pavlov, G. G., et al. 2001, ApJ, 559, L131

Piron, F. 2000, Ph.D. thesis, Univ. Paris XI

Reynolds, S. P. 1998, ApJ, 493, 375

Reynoso, E., et al. 2006, A&A, 449, 243

Schönfelder, V., et al. 2000, in AIP Conf. Proc. 510, Fifth Compton Symp., ed. M. L. McConnell & J. M. Ryan (New York: AIP), 54

Slane, P., et al. 2001, ApJ, 548, 814

Stupar, M., et al. 2005, Adv. Space Res., 35, 1047

Truelove, J. K., McKee, C. F. 1999, ApJS, 120, 299

Tsunemi, H., et al. 2000, PASJ, 52, 887

Ueda, Y., et al. 1999, ApJ, 518, 656

Vincent, P., et al. 2003, in Proc. 28th Int. Cosmic Ray Conf. (Tokyo), 2887

Yamazaki, R., et al. 2007, MNRAS, in press (astro-ph/0601704)